Research Article Vol. 4, No. 12 / December 2017 / Optica 1468

Optical pumped InGaAs/GaAs nano-ridge laser epitaxially grown on a standard 300-mm Si wafer

Yuting Shi,[1,2] Zhechao Wang,[1,2] Joris Van Campenhout,[2] Marianna Pantouvaki,[2] Weiming Guo,[2] Bernardette Kunert,[2] and Dries Van Thourhout[1,2,*]

[1]INTEC Department, Ghent University, Technologiepark-Zwijnaarde 15, 9052 Ghent, Belgium
[2]IMEC, Kapeldreef 75, 3001 Heverlee, Belgium
*Corresponding author: dries.vanthourhout@UGent.be

Received 24 July 2017; revised 24 October 2017; accepted 27 October 2017 (Doc. ID 303094); published 29 November 2017

Fully exploiting the potential of silicon photonics requires high-performance active devices such as lasers, which can be monolithically integrated in a scalable way. However, direct bandgap III–V semiconductors exhibit a large lattice mismatch and/or strongly differing thermal expansion coefficient with silicon. This makes monolithic integration on silicon without introducing excessive defects in the material extremely difficult. The majority of the methods proposed thus far either are not compatible with further low-cost integration or rely on a special substrate. Here we demonstrate monolithic InGaAs/GaAs single-mode nano-ridge lasers directly grown on a standard (001) 300-mm Si wafer. Exploiting the aspect ratio defect trapping technique, unwanted defects are confined to a narrow trench defined in the silicon substrate. The nano-ridge structures subsequently grown out of these trenches are of high crystalline quality as shown by high-resolution transmission electron microscopy analysis and a strong photoluminescence response. They can be controlled in shape by optimizing the growth conditions, which allows us to minimize substrate leakage and maximize confinement in the InGaAs quantum wells providing optical gain. Distributed feedback lasers were fabricated by defining a first-order grating in the nano-ridge. Under pulsed optical pumping, single-mode lasing with side mode suppression over 28 dB was shown, and precise control of the emission wavelength over 60 nm was achieved. This demonstration proves the high quality of the material and provides a credible road towards a CMOS-compatible platform for high-volume manufacturing of silicon photonic integrated circuits, including laser and amplifier devices.

OCIS codes: (140.3490) Lasers, distributed-feedback; (140.3290) Laser arrays; (140.5960) Semiconductor lasers; (160.4236) Nanomaterials.

https://doi.org/10.1364/OPTICA.4.001468

1. INTRODUCTION

Silicon photonic integrated circuits have been intensively studied for over a decade now. By leveraging well-established CMOS manufacturing processes developed initially by the electronics industry, they hold the potential of realizing highly integrated photonic functionality at low cost and in high volumes. However, given the fact that silicon has an indirect bandgap, inhibiting efficient light emission, the lack of a high-performance laser source monolithically integrated on the silicon platform remains a fundamental obstacle in further opening the field to a wider range of applications. Silicon Raman lasers [1] have been demonstrated, but high optical pump power, mitigation of two-photon-absorption-induced optical losses, and low-temperature working conditions are required. Also, the use of strongly doped germanium [2] has been proposed, but the required threshold current densities remain prohibitively high [3]. Exploiting the direct-bandgap alloy GeSn, lasing has been achieved [4] at low temperatures; however, these devices are operating at wavelengths beyond 2 μm and still suffer from low efficiency. Therefore, the integration of direct bandgap III–V semiconductors remains the most promising approach. However, given the large mismatch between silicon ($a_{Si} = 5.431$ Å) and most direct bandgap III–V compounds, which exhibit a lattice constant between 5.6 and 6.5 Å, this remains a huge challenge. The large difference in thermal expansion coefficients and the difference in polarity between Si and III–V compounds further complicates the process. To bypass these issues, several groups demonstrated hybrid III–V/Si lasers whereby III–V epitaxial layers are bonded to an SOI host substrate. This technique is applicable for a wide range of materials and devices [for example, InP-based or GaAs-based Fabry–Perot (FP), disk, distributed-feedback (DFB), distributed Bragg reflector (DBR) lasers], but introduces extra processing steps, making it complex and not compatible with mass production [5]. Therefore, the direct epitaxy of III–V materials on Si is widely believed to be the ultimate solution towards laser integration on the silicon photonics platform. Some research groups have demonstrated lasers fabricated in a thick III–V layer grown on Si,

utilizing a metamorphic buffer layer [6–9] to reduce the defect density introduced by the lattice mismatch. More recently, quantum-dot-based active regions were exploited to realize low-threshold lasers operating at room temperature, benefiting from the fact that quantum dots are less sensitive to dislocations [10–12]. Other approaches to overcome these issues have also been reported in the literature [13–16]. These approaches allow us to reduce the misfit density from a value in the order of 10^8–10^{10} cm^{-2} [17] to a density of 10^5–10^6 cm^{-2}. Although these are impressive results, these values are still two orders of magnitude higher than layers grown on native III–V substrates. In addition, the several-micron-thick buffer layer and the non-selective growth process complicate further integration.

In our earlier work, we demonstrated InP and InP/InGaAs DFB lasers grown on (001) silicon using a selective process [18,19]. This monolithic integration technique does not require a special Si substrate or a thick buffer layer and allows us to achieve high-quality material, as proven through the demonstration of single-mode laser devices operating at room temperature. Nevertheless, to avoid high substrate leakage loss, these laser ridges need to be underetched. This hampers efficient heat dissipation and makes carrier injection for electrical pumping difficult. Therefore, in this work, we investigate if the GaAs/InGaAs nano-ridge structures developed in [20] can overcome these challenges. These nano-ridges are also grown in trenches defined on a standard (001) silicon wafer, but contrary to the previously demonstrated InP lasers, their growth can be extended considerably above the wafer surface. This allows confinement of the optical mode away from the substrate, dramatically reducing optical leakage loss. This in turn makes the underetch process no longer necessary, opening up the path towards better heat dissipation and, potentially, electrical injection.

The growth process of the proposed III–V nano-ridge structure and the analysis of the epitaxial material quality through photoluminescence (PL) and high-resolution transmission electron microscopy (TEM) is described in the next section. In Section 3 we discuss the design and fabrication of single-mode DFB lasers with precisely controlled emission wavelength. The experimental results are presented in Section 4.

2. GaAs NANO-RIDGE

A. GaAs Nano-Ridge Epitaxy

The novel epitaxy approach to integrate GaAs on silicon we report in this paper relies on aspect ratio trapping (ART) [21] of defects in narrow oxide trenches to suppress threading dislocations [22]. Despite the fact that GaAs has a lattice constant of 5.654 Å, resulting in a lattice mismatch as large as 4.1% with Si, we obtained GaAs nano-ridges with very high crystal quality, which can serve as a fully relaxed buffer for the pseudomorphic growth of compressively strained InGaAs quantum wells. The growth starts from an oxide mask on Si, which is obtained by a standard shallow trench isolation (STI) process flow whereby trenches of 5 mm in length and widths varying from 60 to 500 nm are patterned in a 300-nm-thick SiO_2 layer on exact (001) 300-mm Si substrates. There are ten trenches of each configuration, and the ratio of the Si trench surface versus the total area is kept constant to 9%. A V-shaped Si groove with exposed {111} facets is achieved by a tetramethylammonium hydroxide (TMAH) wet-etch step. The purpose of the V-shaped silicon surface at the bottom of the trench is to avoid anti-phase-domain formation. The high-aspect-ratio trench in turn efficiently traps threading dislocations and inclined planar defects by its two vertical SiO_2 sidewalls, stopping defects from going out of the trench into the upper ridge. The growth is carried out using metal-organic vapor phase epitaxy (MOVPE) with tertiarybutyl arsine (TBAs), tertiarybutyl phosphine (TBP), trimethylindium (TMIn), triethylgallium (TEGa), and trimethylgallium (TMGa) as the precursors. The GaAs epitaxy starts with a thin nucleation layer, followed by the growth of the main GaAs structure, first inside and then outside of the trench. A thin GaPAs layer with about 11% P was inserted in the layer stack to induce a slight tensile strain before deposition of the compressively strained quantum wells (QWs). The embedded active region consists of three compressively strained InGaAs QWs with about 20% indium. The growth process is completed by depositing a passivation layer of InGaP covering the full ridge to suppress non-radiative surface recombination and provide better carrier confinement in the lateral direction. By carefully selecting the growth conditions, and thereby controlling the ratio of lateral versus vertical growth, the shape of the ridge and the position of the QWs can be optimized such that it supports a low-loss and high-gain optical mode. Figure 1(a) shows a sketch of the nano-ridge structure. The relevant geometrical parameters are indicated on the cross-sectional high-angle annular dark-field (HAADF)-TEM picture shown in Fig. 1(b) and listed in Table 1 for the characterized structures. The thickness e of the SiO_2 layer is fixed to 300 nm. We find that with increasing trench width d, also the ridge width a, the height b, and the QW position c slightly increase. These variations are believed to result from loading effects during the metal-organic chemical vapor deposition (MOCVD) process. The surface at the bottom of the ridge is inclined at an angle of 54.7°, following the $\{111\}_{Si}$, $\{111\}_{GaAs}$, and $\{111\}_{InGaP}$ planes. The zoomed-in images in Fig. 1(b) show that the trench sidewalls effectively block threading dislocations and that no defects can be observed in the upper ridge structure. Figures 1(c) and 1(d) show a top view of the trench array and a cross section through multiple nano-ridges (trench width 80 nm). These pictures illustrate the uniformity of the epitaxial growth and the flatness of the nano-ridge top surface. More details on the epitaxial deposition can be found in [20,22].

Table 1. GaAs Nano-Ridges Parameters Noted in Fig. 1(b)[a]

d (nm)	a (nm)	b (nm)	c (nm)	n_{eff}	Γ_{QW}
60	364	556	248	3.022	8.84%
80	432	580	274	3.122	9.45%
100	458	602	285	3.167	9.33%
120	530	610	292	3.210	9.6%

[a] d, trench width; a, ridge width; b, ridge height; c, position of the lowest QW; n_{eff}, the effective refractive index of ridge in basic TE optical mode; Γ_{QW}, the basic TE-mode confinement factor in three quantum wells.

B. PL Analysis

The intrinsic material quality of the nano-ridges is evaluated through room-temperature PL analysis. The micro-PL setup consists of a continuous-wave (CW) 532-nm diode-pumped solid-state (DPSS) laser as the pump source; an X50, 0.65-numerical-aperture objective; a 0.25-m monochromator; and a thermo-electric-cooled InGaAs detector. With an illuminated pump intensity 270 W/cm^2, a clear emission peak between 1010 and 1040 nm can be observed from all structures [Fig. 2(a)].

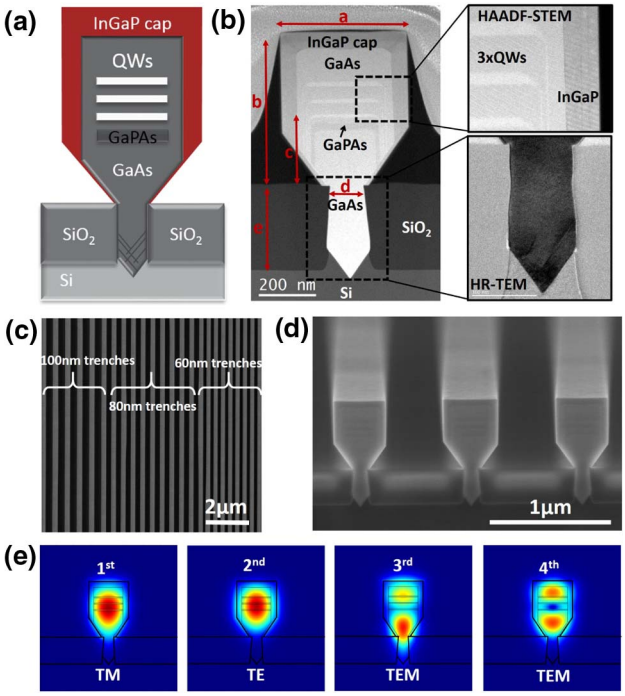

Fig. 1. (a) Sketch of the GaAs nano-ridge laser stack. The inclined lines at trench bottom indicate how planar defects and threading dislocations are trapped inside the trench. (b) HAADF-STEM images of the GaAs nano-ridge waveguide. The upper one shows zoomed-in QWs, barriers, and the passivation layer, while the lower high-resolution (HR) TEM shows that defects are trapped in the V-shaped trench. (c) Top view SEM image of nano-ridge array with trench width from 60 to 100 nm. (d) Tilted cross-section SEM image of three 80-nm trench ridges. (e) The first four modes of the nano-ridge waveguide calculated by finite difference eigenmode (FDE) simulation.

Figure 1(e) shows the first four modes of the nano-ridge configuration with a 100-nm trench width, calculated at the PL peak wavelength of 1030 nm. The first mode is a transverse magnetic (TM)-like mode, which is rather extended in vertical direction and exhibits a relatively high leakage loss towards the Si substrate. The second mode is the basic transverse electric (TE)-like mode, exhibiting the highest confinement in the QWs with $\Gamma_{QW} = 9.33\%$ and a negligible leakage loss $\alpha_{leak} < 5$ dB/cm. Although higher-order TEM modes do exist in the ridge waveguide, for example, the third and fourth modes shown in Fig. 1(e), their high leakage loss and low QW confinement factor should inhibit reaching the lasing threshold, making the structure effectively single mode. The effective refractive index n_{eff} and the QW confinement factor Γ_{QW} of the basic TE-like mode for the ridges with trench widths from 60 to 120 nm are listed in Table 1. Both n_{eff} and Γ_{QW} slightly increase with trench width as the ridge volume increases, resulting in a more confined mode. The leakage loss towards the substrate remains lower than $\alpha_{leak} < 5$ dB/cm for each of these configurations.

C. Laser Design

Starting from the nano-ridge structures described in the previous section, we designed a single-mode DFB laser array incorporating a $\lambda/4$ phase shift section optimized for working with the basic TE mode. The grating is designed using a finite difference time domain (FDTD) solver, taking into account the full three-dimensional configuration. The inset of Fig. 2(b) shows the simulated configuration. The grating depth was limited to 110 nm to avoid etching the top QW layer. The duty cycle and sidewall angle are set to 25% and 65°, respectively, matching the fabricated structures. The period of the gratings is designed such that the stop band overlaps with the measured PL peak. Figure 2(b) shows the calculated reflection spectra for a grating with period 170 nm defined in the nano-ridge with trench width 100 nm. For a 300-period grating, more than 90% reflectivity can be obtained, equivalent with a coupling strength $\kappa L = 3.3$. In the actually fabricated devices, the grating period was swept from 164 to 180 nm for each of the four ridge configurations to accommodate for inaccuracies in the fabrication process and to investigate the relation between lasing wavelength and grating period. In addition, 20 μm away from the first-order grating forming the laser cavity, a 50-period second-order grating was defined to vertically couple out the laser light and allow characterization of the devices in a standard μ–PL setup.

D. Fabrication

After the growth, the GaAs nano-ridge array exhibits considerable surface topography. Therefore, the sample was first planarized by spin coating a layer of 1.7-μm benzocyclobutene (BCB), which then was etched back to the waveguide top surface. Next, the DFB laser was defined by etching a 600-period grating (300 periods each side) in the top surface of the GaAs ridge waveguide with a $\lambda/4$ phase shift section in the middle. The gratings were patterned using electron-beam lithography (EBL). The 200-nm-thick resist layer (AR-P 6200) was directly used as the mask for the inductive coupled plasma (ICP) etching with a $Cl_2/CH_4/Ar$ gas recipe.

Figure 3 shows some details of the fabricated DFB device. Figure 3(a) is a tilted scanning electron microscope (SEM) image taken from the sample surface, showing a group of GaAs ridges with trench width 120, 100, 80, and 60 nm, respectively (10 devices per group). Given the high density of the ridges, only one grating is defined per group of 10. This leaves enough space between two individual DFB devices to facilitate single device characterization and avoid crosstalk, taking into account the lateral extension of the optical pump area of around 5 μm. Figure 3(b) is a zoomed-in image of the central region of the grating with period 170 nm showing the $\lambda/4$ phase shift section. Figure 3(c) shows the second-order grating coupler with period 340 nm. Note that the Fig. 3(c) scale bar is twice as long as the one in Fig. 3(b).

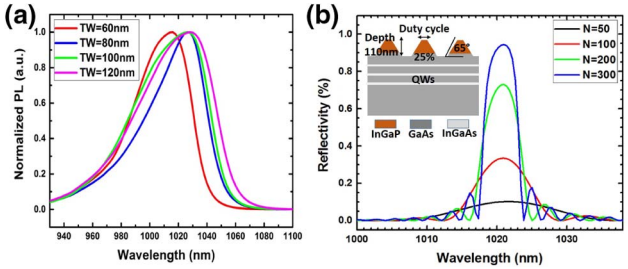

Fig. 2. (a) Normalized room-temperature photoluminescence spectra of nano-ridges with trench width (TW) 60, 80, 100, and 120 nm, respectively. (b) Simulation of Bragg grating reflection spectrum for grating period number increasing from $N = 50$ to $N = 200$. The inset shows a longitudinal cut of the simulated configuration.

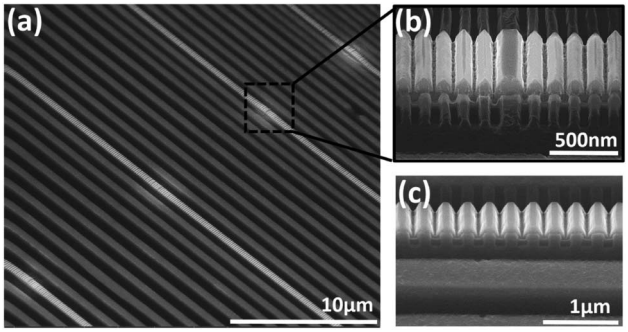

Fig. 3. SEM of (a) a DFB laser array, (b) the zoomed-in $\lambda/4$ phase shift section, and (c) the second-order grating coupler section.

3. EXPERIMENTAL RESULTS

The devices were characterized on the same μ–PL setup used for the PL measurement, but using a Nd:YAG nanosecond pulsed laser (7 ns pulse width, 938 Hz repetition rate, 532 nm wavelength) as the pump source. A rectangular aperture is inserted in the setup to limit the pump spot to a size of 5 μm × 200 μm, covering a single DFB device. The pump intensity is controlled by the combination of a polarizer and a rotating half-wave plate (HWP) added in the setup. A chopper and a lock-in amplifier are used to improve the signal-to-noise ratio. The effective pump power is calculated by measuring the pump intensity and simulating how much of the incident pump light is effectively absorbed in the III–V nano-ridge. For the structures with trench width 100 nm, we found that 65% of the 532-nm pump light is absorbed. Note that given the fact that the pump photon energy of 2.3 eV is higher than that of the bandgap of the InGaP passivation layer (1.90 eV), a considerable part of the pump light is absorbed in this layer, possibly leading to some pump loss due to surface recombination. Also, carriers generated inside the trench are likely to be susceptible to non-radiative recombination given the large defect density close to the GaAs/Si interface, leading to some extra pump loss. Therefore, the effective pump absorption is expected to be less than 65%. Nevertheless, since these effects are hard to quantify, we take a conservative estimate, and all pump powers in the remainder of this paper are normalized with the estimated pump efficiency of 65%.

Figure 4(a) shows the measured spectra of a DFB laser with trench width 100 nm and grating period 170 nm pumped at different powers. When the optical pump power is 17 mW (below threshold), a broad spectrum is observed, centered at 1026 nm with a full width at half-maximum (FWHM) of 60 nm. As the pump power increases to 100 mW ($\sim 3 \times I_{th}$), a peak centered at 1028 nm appears in the spectrum. Finally, at a pump power of 215 mW, the lasing peak reaches more than 28 dB above the background, demonstrating excellent single-mode laser performance. At a pump power of 250 mW, the line width of the laser peak is 1.5 nm (for a monochromator resolution of 0.5 nm), limited by carrier dispersion during the pulsed operation regime. Note that the background PL remains clamped above threshold. Figure 4(b) plots the measured laser light-in light-out curve (L-L curve), both on a logarithm scale and on a linear scale [Fig. 4(b) inset]. The distinct single lasing peak and the clear change in the slope of the L-L curve are strong indicators of laser operation. The pump power at threshold is extracted to be ~37 mW (~33.6 kW/cm^2). Taking into account the measured free carrier decay time for these structures of 400 ps, this allows us to determine that maximum carrier density in the QWs at threshold is 8.74×10^{18}/cm^3, assuming a 100% quantum efficiency for the optical pumping process. In reality, this quantum efficiency is believed to be considerably lower than 100%. For modeling the L-L curve, we used the rate equation model described in [23]. From fitting this model to the experimental data [solid black lines Fig. 4(b)], the spontaneous emission factor β for the nano-ridge laser is found to be ~0.008.

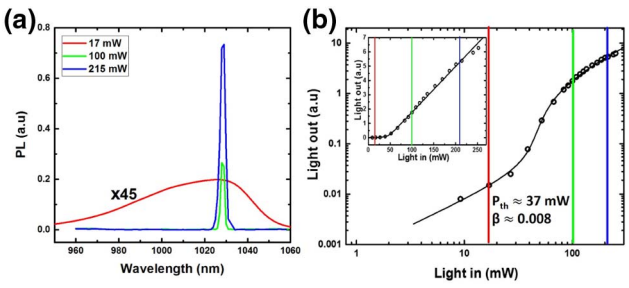

Fig. 4. (a) Room-temperature spectra of a DFB laser under different pump powers (100 nm trench width, 170 nm grating period, and 340 nm second-order grating coupler period). (b) L-L curve on logarithmic and linear (inset) scale of the measured DFB nano-ridge laser. Black circles and solid line represent the experimental data and the rate equations fit, respectively.

Wavelength division multiplexing (WDM), whereby different optical signals with slightly different wavelengths are combined in a single optical waveguide or fiber, is a commonly used approach to increase the capacity of communication links. An essential building block for such systems is an array of single-mode lasers with precisely controlled emission wavelength. To demonstrate the potential of further application of the presented laser, we defined DFB lasers with grating periods varying from 164 to 180 nm for each of the four nano-ridge configurations considered. The grating duty cycle and etch depth were fixed at 25% and 110 nm, respectively. The normalized spectra of four lasers with trench width 60, 80, 100 and 120 nm and fixed grating period of 170 nm are plotted in Fig. 5(a). Each of these devices operates as a single-mode DFB laser. In addition, a clear redshift of the lasing wavelength with increasing trench size is found. As explained above, the increasing trench width results in an increase in ridge volume and, associated with that, a higher effective refractive index of the first TE-like mode (see Table 1). This illustrates the possibility to already tune the DFB-laser emission wavelength during the epitaxy process. Obviously, the lasing

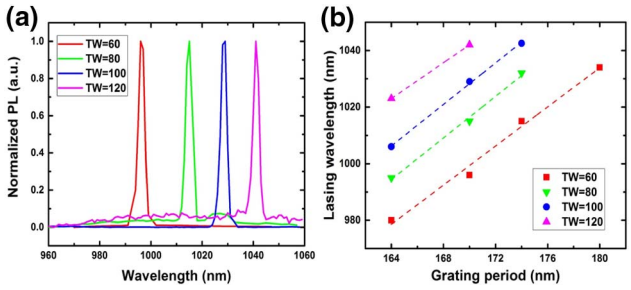

Fig. 5. (a) Measured lasing spectra of DFB laser array with grating period 170 nm. (b) Lasing wavelength versus grating period for trench size varying from 60 to 120 nm.

wavelength can also be controlled through the grating period. Figure 5(b) summarizes the measured lasing wavelength for all different DFB laser configurations, measured at a pump power of 100 mW. One finds that the peak wavelength uniformly shifts with the grating period. The slope of this shift $\frac{\Delta\lambda}{\Delta\Lambda}$ is varying from 3.46 to 3.67 for the different trench sizes, very close to the calculated value $\frac{\Delta\lambda}{\Delta\Lambda} = 3.72$ for the 100-nm trench. The small discrepancy can be attributed to the uncertainty of the refractive index of the III–V ternary alloys in the nano-ridge. Some data for the larger ridges (trench width 80, 100, and 120 nm) at longer grating period (≥174 nm) is missing, as we did not find a lasing peak (expected beyond 1040 nm) for these structures (at pump power 100 mW). This can be explained by the decrease in optical gain for wavelengths above 1040 nm [see also Fig. 2(a)].

4. CONCLUSION

In this paper we report the first InGaAs/GaAs multi-QW single-mode DFB nano-ridge lasers monolithically grown on a standard 300-mm Si wafer. High-quality GaAs nanoridge waveguides with three InGaAs QWs sandwiched inside were grown on (001) Si substrates, relying on the aspect ratio trapping technique and V-shaped trenches to suppress defect formation. Fine-tuning the growth conditions allows us to control the ratio between lateral and vertical growth during the process. This makes it possible to optimize the structures for low substrate leakage loss and high optical gain. The excellent flatness of the nano-ridge side and top surfaces allows the formation of high-quality waveguides without the need for a deep etch process, considerably simplifying the fabrication flow and improving the compatibility with more standard CMOS processes. Starting from this novel epitaxial material, $\lambda/4$ phase-shifted DFB lasers were designed and fabricated by a simple top-down process. Room temperature measurement shows clear single-mode laser operation with a side-mode-suppression ratio better than 28 dB, a line width of 1.5 nm, and a threshold of 37 mW for a 102-μm-long device. Moreover, we demonstrate that the DFB laser emission wavelength can be precisely controlled not only by the grating design, but also by the STI trench width and fine-tuning the epitaxial process, providing more design and fabrication freedom towards optimizing devices for a given application. Most importantly, this successful demonstration proves the quality of the proposed III–V-on-silicon epitaxial process, opening up the road towards high-volume manufacturing of silicon photonic ICs, including III–V lasers and amplifiers, and, given the selectivity of the process, holds the promise of co-integration of active and passive photonic devices based on a mature CMOS platform.

While the current emission wavelength around 1050 nm might be compatible with coupling to silicon nitride waveguides, a next step is obviously to widen the range of achievable emission wavelengths, and in particular to be able to move it to the O band (1260–1360 nm), by increasing the In content in the QW or by the growth of InAs quantum dots. A second step is the demonstration of CW lasing. At this moment, lasing could only be obtained under pulsed optical pumping, which we believe to originate from the high thermal impedance of the structure. Embedding the structure in SiO_2, depositing metal contacts, and more efficient pumping might overcome this. Also, electrical injection should be demonstrated. This will require doping the Si and GaAs layers. Finally, the integration with waveguides is crucial for reaching the final goal, the demonstration of low-cost, highly scalable complex photonic ICs driven by monolithically integrated lasers.

Acknowledgment. This work was supported by IMEC's industry-affiliation R&D Program on Optical I/O and by the Ghent University special research fund.

REFERENCES

1. R. Jones, H. Rong, A. Liu, A. W. Fang, M. J. Paniccia, D. Hak, and O. Cohen, "Net continuous wave optical gain in a low loss silicon-on-insulator waveguide by stimulated Raman scattering," Opt. Express **13**, 519–525 (2005).
2. J. Liu, X. Sun, R. Camacho-Aguilera, L. C. Kimerling, and J. Michel, "Ge-on-Si laser operating at room temperature," Opt. Lett. **35**, 679–681 (2010).
3. M. R. Barget, M. Virgilio, G. Capellini, Y. Yamamoto, and T. Schroeder, "The impact of donors on recombination mechanisms in heavily doped Ge/Si layers," J. Appl. Phys. **121**, 245701 (2017).
4. S. Wirths, R. Geiger, N. von den Driesch, G. Mussler, T. Stoica, S. Mantl, Z. Ikonic, M. Luysberg, S. Chiussi, J. M. Hartmann, H. Sigg, J. Faist, D. Buca, and D. Grützmacher, "Lasing in direct-bandgap GeSn alloy grown on Si," Nat. Photonics **9**, 88–92 (2015).
5. G. Roelkens, A. Abassi, P. Cardile, U. Dave, A. de Groote, Y. de Koninck, S. Dhoore, X. Fu, A. Gassenq, N. Hattasan, Q. Huang, S. Kumari, S. Keyvaninia, B. Kuyken, L. Li, P. Mechet, M. Muneeb, D. Sanchez, H. Shao, T. Spuesens, A. Subramanian, S. Uvin, M. Tassaert, K. van Gasse, J. Verbist, R. Wang, Z. Wang, J. Zhang, J. van Campenhout, X. Yin, J. Bauwelinck, G. Morthier, R. Baets, and D. van Thourhout, "III-V-on-silicon photonic devices for optical communication and sensing," Photonics **2**, 969–1004 (2015).
6. K. Samonji, H. Yonezu, Y. Takagi, K. Iwaki, N. Ohshima, J. Shin, and K. Pak, "Reduction of threading dislocation density in InP-on-Si heteroepitaxy with strained short-period superlattices," Appl. Phys. Lett. **69**, 100–102 (1996).
7. H. Choi, C. Wang, and N. Karam, "GaAs-based diode lasers on Si with increased lifetime obtained by using strained InGaAs active layer," Appl. Phys. Lett. **59**, 2634–2635 (1991).
8. M. E. Groenert, C. W. Leitz, A. J. Pitera, V. Yang, H. Lee, R. J. Ram, and E. A. Fitzgerald, "Monolithic integration of room-temperature cw GaAs/AlGaAs lasers on Si substrates via relaxed graded GeSi buffer layers," J. Appl. Phys. **93**, 362–367 (2003).
9. A. Y. Liu, J. Peters, X. Huang, D. Jung, J. Norman, M. L. Lee, A. C. Gossard, and J. E. Bowers, "Electrically pumped continuous-wave 1.3 μm quantum-dot lasers epitaxially grown on on-axis (001) GaP/Si," Opt. Lett. **42**, 338–341 (2017).
10. Z. Mi, J. Yang, P. Bhattacharya, G. Qin, and Z. Ma, "High-performance quantum dot lasers and integrated optoelectronics on Si," Proc. IEEE **97**, 1239–1249 (2009).
11. Y. Wan, Q. Li, A. Y. Liu, A. C. Gossard, J. E. Bowers, E. L. Hu, and K. M. Lau, "Optically pumped 1.3 μm room-temperature InAs quantum-dot micro-disk lasers directly grown on (001) silicon," Opt. Lett. **41**, 1664–1667 (2016).
12. S. Chen, W. Li, J. Wu, Q. Jiang, M. Tang, S. Shutts, S. N. Elliott, A. Sobiesierski, A. J. Seeds, I. Ross, P. M. Smowton, and H. Liu, "Electrically pumped continuous-wave III– V quantum dot lasers on silicon," Nat. Photonics **10**, 307–311 (2016).
13. Q. Li, K. W. Ng, and K. M. Lau, "Growing antiphase-domain-free GaAs thin films out of highly ordered planar nanowire arrays on exact (001) silicon," Appl. Phys. Lett. **106**, 072105 (2015).
14. T. Frost, S. Jahangir, E. Stark, S. Deshpande, A. Hazari, C. Zhao, B. S. Ooi, and P. Bhattacharya, "Monolithic electrically injected nanowire array edge-emitting laser on (001) silicon," Nano Lett. **14**, 4535–4541 (2014).
15. A. Castellano, L. Cerutti, J. Rodriguez, G. Narcy, A. Garreau, F. Lelarge, and E. Tournié, "Room-temperature continuous-wave operation in the telecom wavelength range of GaSb-based lasers monolithically grown on Si," APL Photon. **2**, 061301 (2017).
16. A. Y. Liu, R. W. Herrick, O. Ueda, P. M. Petroff, A. C. Gossard, and J. E. Bowers, "Reliability of InAs/GaAs quantum dot lasers epitaxially grown on silicon," IEEE J. Sel. Top. Quantum Electron. **21**, 690–697 (2015).
17. H. Kawanami, "Heteroepitaxial technologies of III-V on Si," Solar Energy Mater. Solar Cells **66**, 479–486 (2001).

18. Z. Wang, B. Tian, M. Pantouvaki, W. Guo, P. Absil, J. Van Campenhout, C. Merckling, and D. Van Thourhout, "Room-temperature InP distributed feedback laser array directly grown on silicon," Nat. Photonics **9**, 837–842 (2015).
19. B. Tian, Z. Wang, M. Pantouvaki, P. Absil, J. Van Campenhout, C. Merckling, and D. Van Thourhout, "Room temperature O-band DFB laser array directly grown on (001) silicon," Nano Lett. **17**, 559–564 (2016).
20. B. Kunert, W. Guo, Y. Mols, B. Tian, Z. Wang, Y. Shi, D. Van Thourhout, M. Pantouvaki, J. Van Campenhout, R. Langer, and K. Barla, "III/V nano ridge structures for optical applications on patterned 300 mm silicon substrate," Appl. Phys. Lett. **109**, 091101 (2016).
21. J. Li, J. Bai, C. Major, M. Carroll, A. Lochtefeld, and Z. Shellenbarger, "Defect reduction of GaAs/Si epitaxy by aspect ratio trapping," J. Appl. Phys. **103**, 106102 (2008).
22. B. Kunert, W. Guo, Y. Mols, R. Langer, and K. Barla, "(Invited) integration of III/V hetero-structures by selective area growth on Si for nano-and optoelectronics," ECS Trans. **75**, 409–419 (2016).
23. K. Shore and M. Ogura, "Threshold characteristics of microcavity semiconductor lasers," Opt. Quantum Electron. **24**, S209–S213 (1992).